The Astrophysical Journal, 574:709–718, 2002 August 1

THE SPATIAL DISTRIBUTION OF THE FAR-INFRARED EMISSION IN NGC 253

V. P. Melo, A. M. Pérez García, J. A. Acosta-Pulido, C. Muñoz-Tuñón, and J. M. Rodríguez Espinosa
Instituto de Astrofísica de Canarias, E-38200 La Laguna, Tenerife, Spain;
vmelo@ll.iac.es, apg@ll.iac.es, jap@ll.iac.es, cmt@ll.iac.es, jre@ll.iac.es
Received 2001 October 1; accepted 2002 April 8

ABSTRACT

We study the far-infrared emission properties of the nearby starburst galaxy NGC 253 based on *IRAS* maps and an ISOPHOT map at 180 μm. Based on the analysis of the light profiles, we have been able to identify three main structural components: an unresolved nuclear component, an exponential disk, and a kiloparsec-scale bar. In addition, we also found a ring structure at the end of the bar that is particularly conspicuous at 12 μm. The spectral energy distribution of each morphological component has been modeled as thermal dust emission at different temperatures. The unresolved nuclear component is dominated by cold dust emission ($T \simeq 50$ K), whereas the disk emission is dominated by very cold dust ($T \simeq 16$ K) plus a contribution from cold dust ($T \simeq 55$ K). The bar emission corresponds mainly to cold dust ($T \simeq 23$ K) plus a warm component ($T \simeq 148$ K). We detect an extension of the disk emission due to very cold dust, which contributes a large fraction (94%) of the total dust mass of the galaxy. The estimated total dust mass is $8.2 \times 10^7\ M_\odot$.

Subject headings: dust, extinction — galaxies: individual (NGC 253) — galaxies: photometry — galaxies: starburst — galaxies: structure — infrared: galaxies

1. INTRODUCTION

Much of our knowledge about the infrared (IR) emission from galaxies comes from their total emission fluxes. Models of the spectral energy distribution (SED) from UV to radio wavelengths have been successful in reproducing the observations in a variety of galaxies, from normal to starburst types (Devriendt, Guiderdoni, & Sadat 1999; Silva et al. 1998; Efstathiou, Rowan-Robinson, & Siebenmorgen 2000). Nevertheless, there are still some controversial aspects that need to be addressed, such as:

1. Whether heating of dust by ultraviolet photons from young stars is the dominant source of the far-IR (FIR) emission (Devereux et al. 1994) or there is a noticeable contribution from nonionizing photons from bulge and disk stars (Walterbos & Schwering 1987; Xu & Helou 1996; Mayya & Rengarajan 1997).
2. The inner gas to warm dust mass ratios. In external galaxies these are about 5–6 times the local Galactic value (Devereux & Young 1990), implying a deficit of cold dust. This can be attributed to a lack of data beyond 100 μm, yielding both an overestimate of the dust temperature and an underestimate of cold dust masses hidden by other, more energetically important, components.
3. The extension of dust disks, as compared to stellar disks observed in the optical bands. Engargiola (1991) and Engargiola & Harper (1992) found that the scale length of stellar disk is similar to or larger than the dust disk observed at 160 μm continuum. However, recent work seems to support dust disks larger than the stellar ones by factors from 1.4 to 2 (Davies et al. 1997; Alton et al. 1998b; Xilouris et al. 1999).
4. The opacity of the disk in spiral galaxies. Disney, Davies, & Phillipps (1989) suggested that the spiral galaxies could be optically thick. However, more recent works indicate only moderately opaque disks (Xilouris et al. 1999). This feature has relevant cosmological implications, giving different degrees of extinction to be accounted for in the cosmic background.

Adding spatial resolution to the study of the far-IR emission from galaxies certainly helps in resolving most of these controversial points. This has been possible only in a limited number of nearby galaxies, thanks to the instruments on board the NASA Kuiper Airborne Observatory (KAO) and to the improved resolution ($\sim 1'$) of maps obtained with the *Infrared Astronomical Satellite* (*IRAS*) and processed by the HIRES algorithm (Aumann, Fowler, & Melnyk 1990; Rice 1993). Engargiola (1991) has studied the FIR continuum distributions of NGC 6946 from 60 to 200 μm, using *IRAS* and NASA Kuiper Airborne Observatory data, showing that the light distribution reveals discrete sources, coinciding with giant H II regions, superimposed on an unresolved, exponential, dust emission background. The brightness profiles were separated into a nuclear starburst plus an exponential disk. The nuclear and the disk SEDs were described as modified blackbody sources at $T \sim 40$ and ~ 15 K, respectively. Far-IR maps of the quiescent spiral galaxies M31 and NGC 4565 have been studied by Xu & Helou (1996) and Engargiola & Harper (1992), respectively. In both cases they could distinguish warm dust tracing the spiral arms, superimposed on a diffuse, cool dust emission corresponding to the disk. They also found that old stars contribute an important fraction of the heating of the dust.

More recently, with the launch of the *Infrared Space Observatory* (*ISO*), with its onboard instrument ISOPHOT, maps of similar or better resolution have been obtained up to 200 μm, allowing more detailed studies of various physical quantities related to the FIR emission of galaxies. Questions concerning the dust and temperature distributions, the structural components followed by the dust distribution, the existence of very cold dust emission, and the physical extent of the disks can all be addressed. Haas et al. (1999) have mapped the FIR emission of M31 at 175 μm using ISOPHOT data, showing the importance of the contribution of cold dust to the total mass of the galaxy.

Relevant advances also come from the theoretical front. Most current models are able to reproduce the main features of the far-IR emission from different types of galaxies

consistently with other wavelength ranges dominated by the stellar radiation. For instance, Devriendt et al. (1999) developed successful models that take into account the evolution of the stellar population, as well as extinction and emission of dust, in a self-consistent way. On the other hand, Bianchi, Davies, & Alton (2000) constructed bidimensional models to predict the dust-reprocessed FIR output in spiral galaxies corresponding to different stellar and dust geometries. These models could explain the observed far-IR SED from spiral galaxies only when dust disks are optically thick. However, they failed to reproduce the large far-IR scale lengths suggested by recent far-IR observations (Alton et al. 1998b).

Because of its proximity, NGC 253 is a good candidate for detailed studies at any wavelength range. Its angular size in the visible range is $27\farcm5 \times 6\farcm8$. It is classified as a spiral galaxy of type SAB(s)c and is seen almost edge-on. Throughout this paper, we adopt a distance of $D = 3.4$ Mpc (Sandage & Tammann 1975), implying a scale of 16.5 pc arcsec^{-1}. NGC 253 is considered a prototype nuclear starburst galaxy, exhibiting strong IR emission ($L_{\rm IR} \sim 2 \times 10^{10}$ $L_{\odot}$), that is, an ideal target for IR studies. In this paper, we analyze maps of NGC 253 from 12 to 180 μm. We are able to separate the far-IR emission into its morphological components. The SED of each component was been modeled in terms of blackbody emission.

2. MID- AND FAR-IR MAPS

The ISOPHOT (Lemke et al. 1996) data at 180 μm were retrieved from the *ISO* Data Archive.[1] The map was constructed in undersampled raster mode, with a step of 180″, using the C200 camera, which consists of a 2×2 pixel array (the pixel size is 89″). The data were reduced using PIA version 9.1 (Gabriel et al. 1997), and the following corrections were applied: ramp linearization, deglitching at the ramp and signal levels, and dark-signal subtraction. Only the last 60% of the signal at each raster position was retained, in order to minimize transient effects. The flux calibration was performed using the internal calibration lamps, although the final calibration was determined by comparing the sky background measurement in the 180 μm ISOPHOT map with background measurements from *COBE*/DIRBE maps. A scaling factor of 1.48 has to be applied to the ISOPHOT data in order to match the two background measurements. Two pixels of the C200 array were saturated when crossing the nucleus of the galaxy. The values at these map positions were obtained by interpolation from the neighboring pixels. This fact may produce a broadening of the light profile at the center of the galaxy and probably results in an underestimate of the nuclear contribution. The map reconstruction was performed within PIA, using the trigrid algorithm. We estimate the actual resolution of this map to be ~180″, as a result of the poor raster sampling. The isocontours of the 180 μm image, overlaid on a *B*-band (MPG/ESO 2.2 m + WFI optical) image,[2] are presented in Figure 1. The main features present in the optical image can also be recognized in the 180 μm map. However, the morphology at 180 μm is slightly different than that observed in the other IR bands. The emission along the minor axis extends up to 10 kpc from the nucleus. This extended emission can be associated with a cold dust halo. Additional evidence was found in our analysis of the strip maps perpendicular to the disk (Pérez García et al. 2001) The same conclusion has been reached by Radovich, Kahanpää, & Lemke (2001). A similar morphology has been reported from *ROSAT* X-ray observations by Pietsch et al. (2000).

We retrieved *IRAS* maps at 12, 25, 60, and 100 μm from the Infrared Processing and Analysis Center at Caltech (IPAC). The data retrieved were processed using the HIRES algorithm, which is based on the maximum correlation method (Aumann et al. 1990), to produce images with improved spatial resolution. The resolution of these *IRAS* maps ranges from 1′ at 12 and 25 μm to 1.′7 at 100 μm. Unfortunately, the low-level emission seen in the *IRAS* maps cannot be used because of the spurious structures, caused at 12 and 25 μm (see Fig. 2) by detector hysteresis after crossing the bright nucleus and at 60 and 100 μm by reflected emission off the *IRAS* secondary spider (Rice 1993).

Very recently, Radovich et al. (2001) have studied the far-IR emission of NGC 253 using *IRAS* and *ISO* data, as well as a numerical radiative transfer model. Their main aim was detecting FIR emission above the disk that might be connected with outflows and/or supergalactic winds. These authors have also shown the need for an extended dust disk.

3. RESULTS

3.1. *IR Luminosity Profiles*

For all maps, we obtained surface brightness profiles by azimuthally averaging over elliptical annuli. We fitted the isocontours of surface brightness with the ELLIPSE task in IRAF,[3] which uses the algorithm described in Jedrzejewski (1987). The spatial interval between two consecutive isophotes is equal to the pixel size in each filter, but averaged over an annulus of width close to the resolution in each filter. Figure 2 shows the family of ellipses fitted for two filters, 12 and 25 μm. At first glance, it can be noted how the isophotal twisting delineates the presence of a bar and a ring at the circumnuclear region (discussed below). The brightness profiles, ellipticities (ϵ), and position angles (P.A.) in all filters as a function of radial distance from the galaxy center are shown in Figure 3. Figure 4 shows the light profiles normalized to the central peak, to facilitate the comparison at the different wavelengths. The brightness profiles show similar behavior in all the IR filters, with the exception of the 180 μm profile. Two different slopes are clearly distinguished, a steep profile from the central peak out to about 2′–4′ and from there on a flattened profile that samples the disk of the galaxy (see Fig. 4). The IR emission concentrates at different radii, depending on the wavelength: the sharpness of the luminosity profiles from 12 to 100 μm reflects the predominance of the warm dust emission associated with the starburst activity at the galaxy center. In the outer parts,

[1] Based on observations with *ISO*, an ESA project with instruments funded by ESA member states (especially the PI countries: France, Germany, the Netherlands, and the United Kingdom) and with the participation of ISAS and NASA.

[2] Obtained with the Wide Field Imager (full field) at the MPG/ESO 2.2 m telescope and retrieved from the ESO archive.

[3] IRAF is the Image Reduction and Analysis Facility, a general-purpose software system for the reduction and analysis of scientific data. IRAF is written and supported by the IRAF programming group at the National Optical Astronomy Observatory (NOAO).

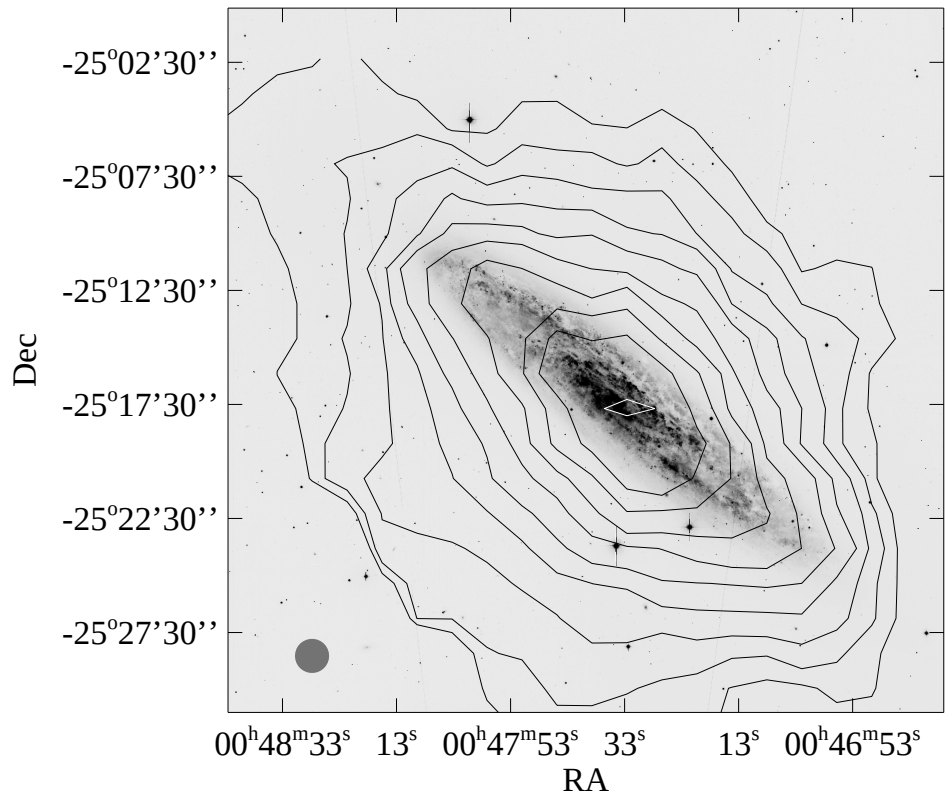

FIG. 1.—Contours of the ISOPHOT 180 μm map overplotted on a *B*-band image (from the ESO database). The instrumental resolution is shown at the bottom left corner. Contours represent luminosity in logarithmic scale and range from 3 σ to the maximum value. Contours are separated by a factor of 1.8 from 1 to 230 MJy sr^{-1}.

the disk is the dominant structure. In contrast, the luminosity profile at 180 μm appears flatter than the other profiles, following an exponential disk profile behavior at all radii. No central region can be distinguished in the 180 μm profile.

The absence of a central peak at 180 μm is probably a consequence of the lower prominence of the nucleus at that wavelength, although the saturation problems mentioned above likely blur the central peak. Remarkably, the extension and the decay of the light profile at 180 μm are comparable to those measured in the *B* band (Pence 1980; see Fig. 4), although the slope beyond 15 kpc is slightly flatter at 180 μm than at the *B* band. This fact may indicate an extended disk of very cold dust (Radovich et al. 2001).

More structures can be distinguished in the brightness profiles. At a distance of $\sim$3.5 kpc, there is a shoulder in the 12 μm profile, which is also evident in the 25 μm profile; this feature coincides with the end of the inner disk detected by Scoville et al. (1985), which we have also identified as a ring structure (discussed in § 3.2). There are other findings that support this identification: an excess of millimeter CO emission at 3.5 kpc along the semimajor axis, reported by Scoville et al. (1985) and more recently by Sorai et al. (2000); and an Hα image shows a remarkable ring structure with radius of 2.′7 (Hoopes, Walterbos, & Greenawalt 1996). The prominent hump observed in the *B* band at a distance between 6′ and 12′ along the semimajor axis is marginally present in the 100 μm profile. The hump at the *B* band has been attributed to young stars and H II regions in the spiral arms (Pence 1980). Note that in the other *IRAS* filters we cannot see the hump, probably because of noise introduced by spurious structures at low flux levels.

The P.A. and the ellipticity also vary considerably with galactocentric distance. In particular, the 12 μm light profile shows drastic changes in both ellipticity and P.A. at radii between 2 and 3.5 kpc. The ellipticity increases from the center to a maximum value of 0.8 at a distance of 3.5 kpc, where it suddenly decreases to a value of 0.5; from there outward, the ellipticity approaches the disk value of 0.75. Simultaneously, the P.A. changes from 70° to 60° at 2 kpc, falling to the outer-disk average value of 52.°3 at a distance of 3.5 kpc. The 25 μm profile shows a behavior similar to that at 12 μm, although the P.A. remains constant at 70° up to 3.5 kpc. We identify these features with the presence of a bar whose existence has been reported by other authors (Pence 1980; Scoville et al. 1985; Forbes & DePoy 1992). Both the orientation and the extension match well the values reported in the near-IR: Scoville et al. (1985) found in a 2.2 μm map an elongated barlike structure with a radius $\sim$1.98 kpc, oriented at P.A. = 68°, within an inner disk that extends out to $\sim$2.97 kpc; Forbes & DePoy (1992) found in an *H*-band image a bar oriented at $\sim$70° and extending 2.48 kpc. The barred nature of this galaxy is obvious in the near-IR (Scoville et al. 1985) and also quite evident in the 2MASS Atlas Image Gallery mosaic of this galaxy.[4] Moving outward, the P.A. and ellipticity reach the same asymptotic limiting values for the different filters, within the errors. We obtain for the ellipticity the average value 0.79 ± 0.10, which corresponds to a galaxy inclination of $i \simeq 78° \pm 6°$, and P.A.

[4] This image (*J*, *H*, and K_s composite) is available electronically at http://www.ipac.caltech.edu/2mass/gallery/images_galaxies.html.

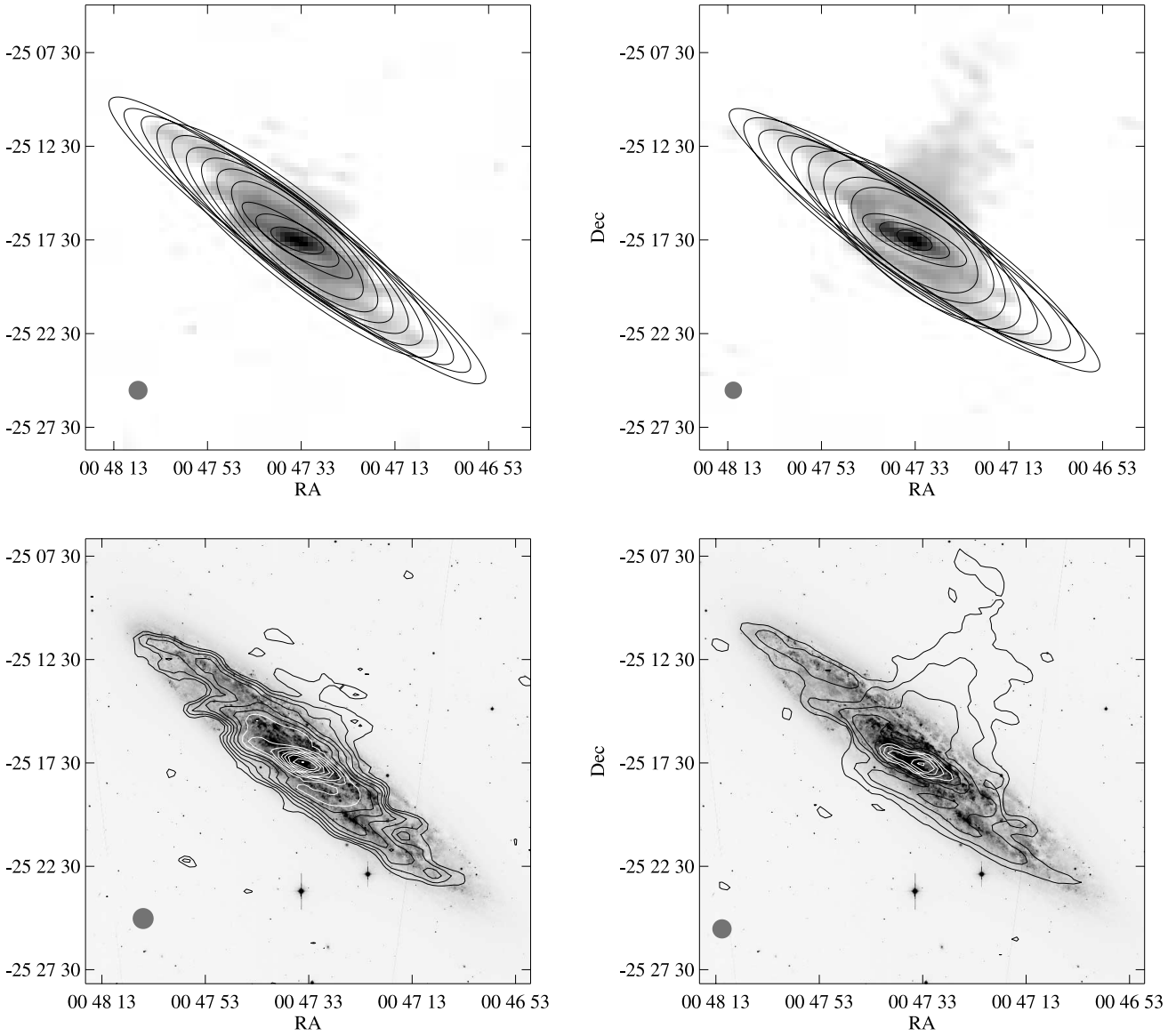

FIG. 2.—*Bottom left*: Contours of the *IRAS* image at 12 μm overplotted on a *B*-band image (from the ESO database). Contours represent luminosity in logarithmic scale and range from 5 σ to the maximum value. Contours are separated by a factor 1.8 from 1.3 to 340 MJy sr^{-1}. *Top left*: *IRAS* image at 12 μm with overlaid ellipse fits. *Top right*: *IRAS* image at 25 μm, with overlaid ellipse fits. *Bottom right*: Contours represent luminosity in logarithmic scale and range from 5 σ to the maximum value. Contours are separated by a factor 1.8 from 1.5 to 2100 MJy sr^{-1}. The instrumental resolution is shown at the bottom left corner of each panel.

$50° \pm 7°$, representing the disk. These values are in good agreement with those obtained by Pence (1980) using optical data (P.A. $= 51°$, $i \simeq 78\overset{\circ}{.}4 \pm 0\overset{\circ}{.}3$). As the resolution decreases—moving to longer wavelengths—details of the isophotes at the inner part become less representative. At 180 μm, the P.A. reaches values in the outer parts similar to those at 12, 25, 60, and 100 μm. However, the ellipticity remains lower, the isophotes being rounder. This is consistent with the detection of a cold dust halo. This halo is not detected at other wavelengths, except at 100 μm, which shows a slightly lower ellipticity. This is consistent with the work by Alton, Davies, & Trewhella (1998a), who fail to detect dust emission above the disk using *IRAS* images from edge-on galaxies.

We have also looked at the variation of the IR colors with galactocentric distance (see Fig. 5). The mid- and far-IR color ratios approximately describe the origin of the dust emission at these wavelengths (Helou 2000; Telesco 1993). In a simplified scenario, the IR emission of a relatively normal galaxy can be described as a composite of two spectral components (Helou 1986): blackbody emission from classical grains in temperature equilibrium, heated by the interstellar radiation field dominating in the far-IR; and very small grains and polycyclic aromatic hydrocarbon (PAH) molecules transiently heated to high temperatures by the absorption of single energetic photons produced in star-forming regions. As a result, starbursts have warmer 60/100 μm color temperatures and cooler 12/25 μm color temperatures. The more active starbursts exhibit bluer 25/60 μm and 60/100 μm colors, corresponding to warmer dust in high-temperature equilibrium. As a guide, we have superposed for all colors the typical values of two model components: the disk (D) and the starburst (SB). These models were used to synthesize the observed far-IR spectra of many

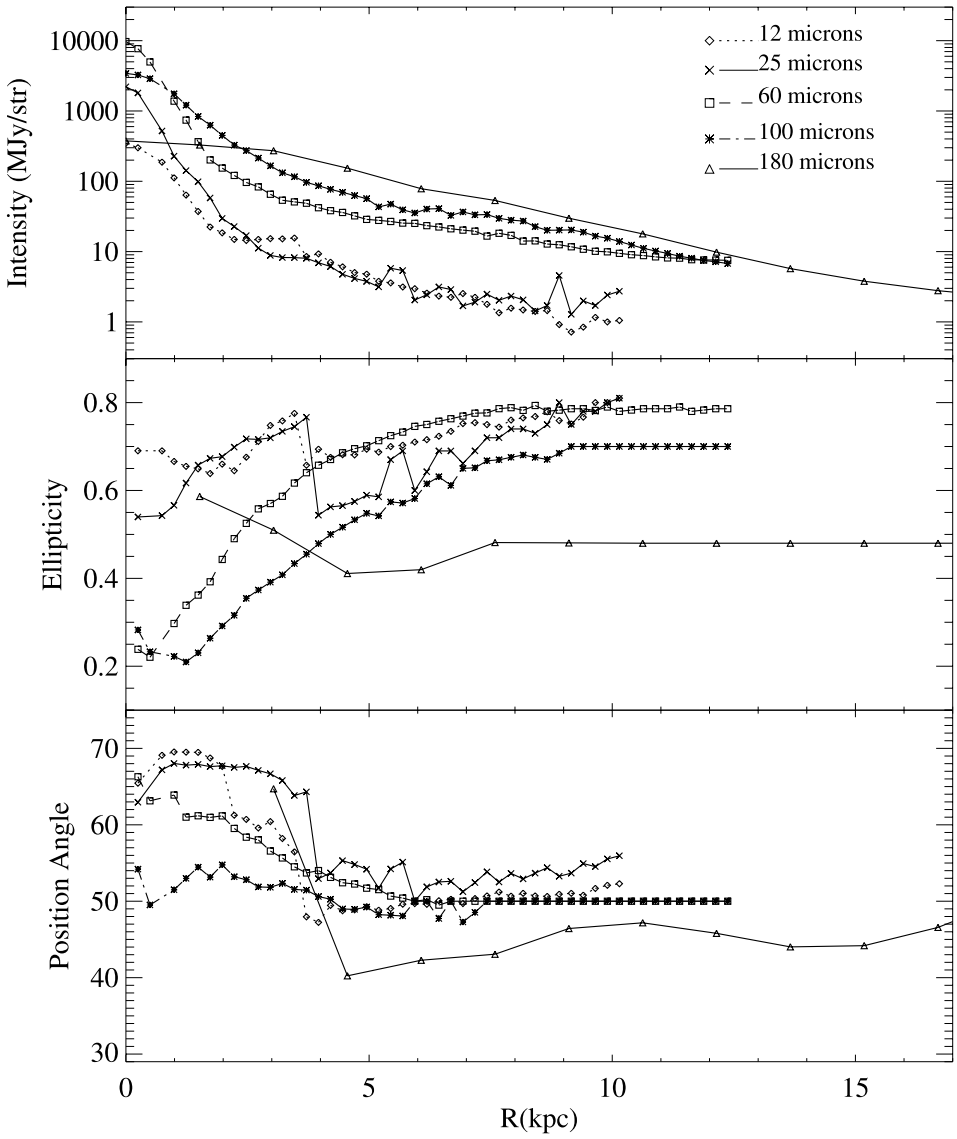

FIG. 3.—Radial variation of the elliptical isophote parameters from the different filters vs. radial distance from the center for 12 μm (*dotted line*), 25 μm (*double-dot–dashed line*), 60 μm (*dashed line*), 100 μm (*dot-dashed line*), and 180 μm (*solid line*): luminosity profiles (*top*), ellipticity (*middle*), and P.A. (*bottom*).

IRAS galaxies by Rowan-Robinson & Crawford (1989). The first thing to notice is that in the outer regions, all colors are typical of disk emission. The 12/25 μm color index shows a strong peak, coincident with well-identified morphological features (described in § 3.2). In the innermost regions, this color matches that of typical starburst galaxies. Around 3–4 kpc, there is a strong color increase slightly beyond the end of the bar, at the location of the ring detected in our profile separation (as described below). The origin of this color enhancement can be related to an intense PAH emission associated with the ring of molecular gas mentioned above (Scoville et al. 1985; Sorai et al. 2000). The 25/60 μm color index shows a smoother trend. An interesting feature appears around 2 kpc, coincident with the head of the barlike structure, that might be another indication that star formation is taking place there. The 60/100 μm and 100/180 μm color indexes have an absolute maximum at the center of the galaxy, as corresponds to the central starburst activity. The 60/100 μm color index shows a small increase coincident with the beginning of the spiral arm. This is interpreted as an increase in dust temperature due to star formation in large H II regions, as observed by Engargiola (1991) in NGC 6946.

3.2. *Surface Brightness Profile Decomposition*

The best-fit structural components to the radial light profiles at 12, 25, 60, 100, and 180 μm are shown in Figure 6. Initially, we tried a morphological separation of the profiles into two components: an unresolved source corresponding to the point-spread function (PSF; for the *IRAS* maps we use Gaussian functions and for the ISOPHOT map a model PSF) and an exponential disk that mainly accounts for the external regions of the galaxy. The resolution of the 180 μm map is not sharp enough to separate any components other than the exponential disk. A bulge component was not included, because it cannot be sampled with the limited resolution of our maps. Forbes & DePoy (1992) found an effec-

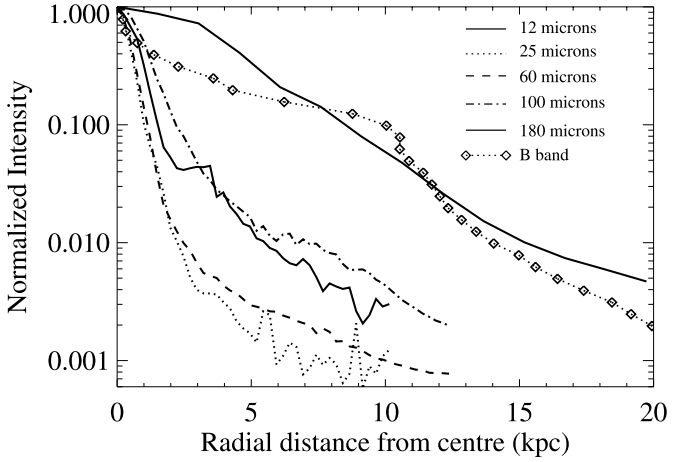

FIG. 4.—Normalized luminosity profiles at 12 μm (*triple-dot–dashed line*), 25 μm (*dotted line*), 60 μm (*dashed line*), 100 μm (*dot-dashed line*), and 180 μm (*solid line*). The luminosity profile in the *B* band is also shown (*dotted line with diamonds*). The *B*-band data are taken from Pence (1980). Note the slow decay of the 180 μm emission, comparable to that of the *B* emission, in contrast to the sharp profiles in the range 12–100 μm.

tive radius (10″) for the bulge that is well below our resolution limit, so its contribution will be implicitly included in the unresolved component. The analytic profiles were convolved using the corresponding PSF for each filter, before

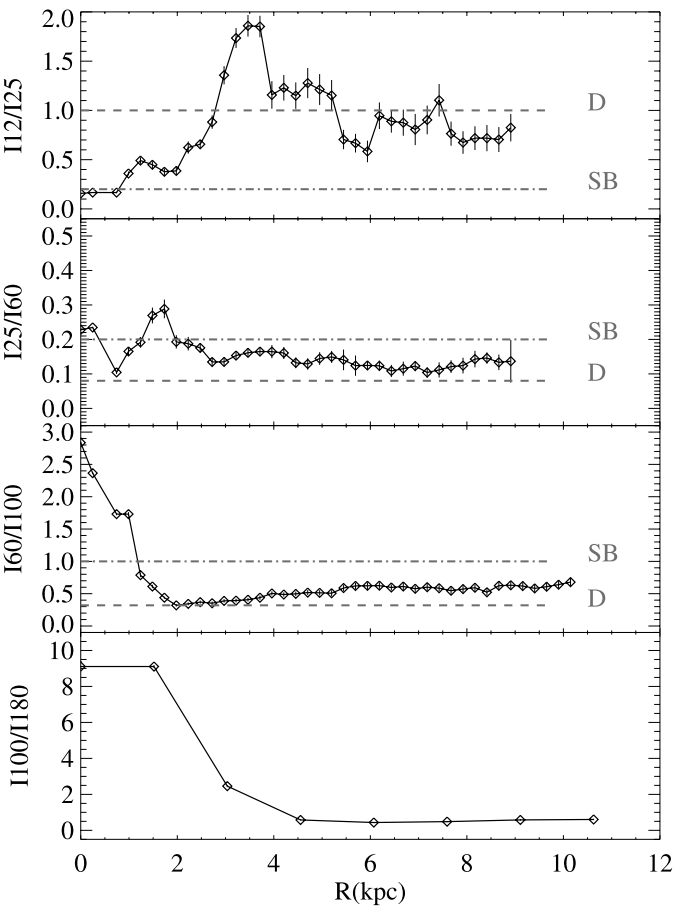

FIG. 5.—Variation of IR colors along the major axis of elliptical isophotes. Data points are smoothed to the worse resolution in each color combination. Horizontal lines are the values expected for starbursts (SB) and disks (D) from Rowan-Robinson & Crawford (1989).

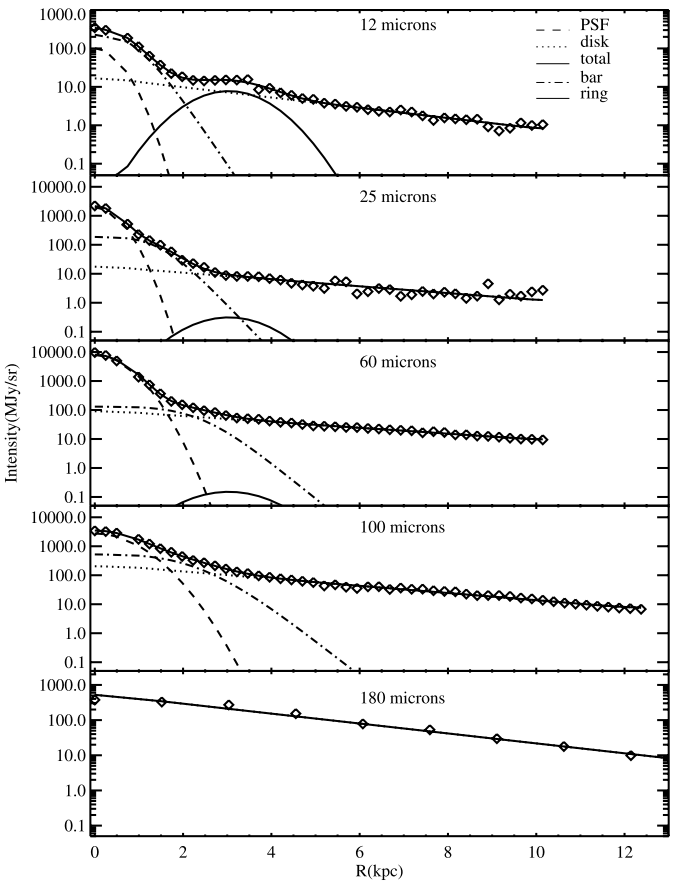

FIG. 6.—Surface brightness profile decomposition for all bands: 12, 25, 60, 100, and 180 μm (*top to bottom*). The unresolved nuclear component (*dashed line*) dominates the central emission, except at 180 μm (see text). The bar (*dot-dashed line*) is clearly distinguished up to 100 μm. The disk (*dotted line*) always appears at the outermost isophotes. The ring (*triple-dot–dashed line*) is clearly seen only at 12 and 25 μm.

the fitting. A third component was introduced to improve the matching of the models with the observed profiles following the indications of the presence of a bar discussed in § 3.1. For this component we have taken a flat bar profile:

$$I_{\rm bar}(r) = \frac{I_{\rm bar}}{1 + \exp[(r - r_{\rm bar})/l_{\rm bar}]}$$

(Prieto et al. 1997), where $I_{\rm bar}$ is the amplitude, $r_{\rm bar}$ is the length, and $l_{\rm bar}$ is the downward gradient.

In addition, the 12 μm luminosity profile shows a conspicuous maximum around 3.′5, at the position where a strong decrease in the ellipticity and a noticeable variation in the P.A. are found. We identify this feature with a ring at the end of the bar, which also coincides with the maximum extent of the inner disk identified by Scoville et al. (1985). This structure can be related to the molecular and Hα rings detected by Sorai et al. (2000) and Hoopes et al. (1996). A ring structure can be described by a Gaussian profile (Buta 1996) as

$$I_{\rm ring}(r) = I_{\rm ring} \exp\left[-\frac{1}{2}\left(\frac{r - r_{\rm ring}}{l_{\rm ring}}\right)^2\right],$$

where $I_{\rm ring}$ is the amplitude, $r_{\rm ring}$ is the center, and $l_{\rm ring}$ is the width.

TABLE 1
STRUCTURAL PARAMETERS

λ (μm)	I_{PSF} (MJy sr^{-1})	I_{disk} (MJy sr^{-1})	r_{disk} (kpc)	I_{bar} (MJy sr^{-1})	r_{bar} (kpc)	l_{bar} (kpc)	I_{ring} (MJy sr^{-1})	r_{ring} (kpc)	l_{ring} (kpc)
12.....	100 ± 20	18 ± 2	3.2 ± 0.3	280 ± 40	0.73 ± 0.08	0.26 ± 0.03	8.5 ± 0.9	3.0 ± 0.3	0.69 ± 0.11
25.....	1950 ± 200	19 ± 2	3.7 ± 0.4	190 ± 20	1.34 ± 0.14	0.28 ± 0.03	0.3 ± 0.4	3.0 ± 0.3	0.69 ± 0.11
60.....	7880 ± 790	99 ± 10	4.3 ± 0.4	130 ± 20	2.1 ± 0.2	0.35 ± 0.12	0.2 ± 3.9	3.0 ± 0.3	0.69 ± 0.11
100.....	2760 ± 280	230 ± 20	3.5 ± 0.4	550 ± 70	1.9 ± 0.2	0.37 ± 0.04	$4.8e{-4} \pm 2.4e{-4}$	3.0 ± 0.3	0.69 ± 0.11
180.....	...	550 ± 170	3.1 ± 0.9	...	...	...	...	...	...

The ring can still be recognized in the intensity profile at 25 μm, but it disappears at 60, 100, and 180 μm. Nevertheless, we have introduced this morphological component in the decomposition of the 25 and 60 μm profiles, although the radial distance (r_{ring}) and the width (l_{ring}) are fixed to that at 12 μm, in order to obtain a meaningful fit. We have checked that introducing this component at the other wavelengths (60 and 100 μm) does not change the fit results, which are compatible with a very low amplitude for it. The uncertainty of the amplitude of the ring at 60 μm is compatible with non-detection (see Table 1) of the mentioned ring.

The resulting parameters for the different morphological components and filters are given in Table 1. During the fitting process all parameters were allowed to vary freely, except for the radial distance and width of the ring, as mentioned above. The uncertainties in the parameter values were computed using a bootstrapping technique. This procedure is based on a Monte Carlo simulation: new light profiles are obtained by perturbation of each measured profile value, using a normal distribution of the same width as the error of that point. New fit parameters are determined for each simulated profile (usually 50 simulations), and the uncertainty of each parameter is taken as the standard deviation of the resulting values.

The disk scale lengths obtained in all the examined maps are very similar and have a mean value of 3.63 kpc. This is very close to the value of 3.32 kpc obtained in the *B* band by Pence (1980). Puche & Carignan (1991) found in H I observations a disk scale length of 3.41 kpc. However, Forbes & DePoy (1992) obtained in the *H* band a disk scale length of 2.65 kpc along the semimajor axis. The smaller scale length observed in the *H* band, if confirmed at *J* and *K*, could be attributed either to high extinction at the inner parts or to the presence of very high temperature, small dust grains emitting in the near-IR. An important result is that both the stellar disk scale length (Pence 1980) and the dust scale length are similar, which is not in agreement with the findings of Radovich et al. (2001) based on radiative transfer models of this galaxy.

3.3. *Spectral Energy Distributions of the Structural Components*

The IR SED of the morphological components, namely, the unresolved nucleus, the disk, and the bar found in the previous section, are displayed in Figure 7. For each filter and each morphological component, we represent the emission integrated over the galaxy. The uncertainty of the emission from any component is determined from the uncertainty of the amplitude. The global emission of each morphological component has been modeled as the combination of the emission from emissivity-weighted blackbody components (Hildebrand 1983). An emissivity index of 2 has been adopted. The best-fitting blackbody temperatures are compiled in Table 2. The uncertainties in the temperature and scaling factor of each blackbody were computed using the bootstrapping technique, similar to what was done for the profile decomposition.

The SED of the unresolved nuclear component can be modeled as a cold ($T \simeq 49$ K) component. The cold component has a temperature typical of dust heated in star-forming regions. This component is present in nearly all classes of galaxies, including normal, starburst, and even active galaxies (Knapp et al. 1996; Chini, Krügel, & Kreysa 1992; Klaas et al. 1997; Pérez García & Rodríguez Espinosa 2001). There is an excess at 12 μm, which is likely due to a combination of PAH and very small grain emission. In fact, PAH emission has been detected at the central regions of NGC 253 (Pérez García et al. 2001; Dudley & Wynn-Williams 1999; Keto et al. 1999).

The SED of the disk component is explained by a combination of a cold ($T \simeq 55$ K) and a very cold ($T \simeq 15$ K) component. The warmer component is again due to dust heated in H II regions and OB associations populating the arms of the disk. The temperature of the very cold compo-

TABLE 2
DERIVED PROPERTIES OF THE IR STRUCTURAL COMPONENTS

Component	T (K)	F_{IR} (10^{-8} ergs s^{-1} cm^{-2})	L_{IR} ($10^9 L_\odot$)	Dust Mass ($10^6 M_\odot$)	SFR ($M_\odot$ yr^{-1})
PSF.....	49.4 ± 0.9	5.77 ± 0.03	20.9 ± 1.5	0.21 ± 0.02	3.5 ± 0.3
Disk.....	55 ± 15	1.097 ± 0.011	4.0 ± 1.3	0.02 ± 0.03	0.7 ± 0.2
	15.9 ± 2.1	2.4 ± 1.6	8 ± 3	77 ± 58	...
Bar.....	148 ± 74	0.8 ± 0.5	3 ± 2	$\ll 1$	...
	23 ± 12	1.4 ± 0.9	5 ± 3	5 ± 14	0.8 ± 0.6
Total.....	...	11.4 ± 1.5	41.1 ± 1.6	82 ± 7	5 ± 1

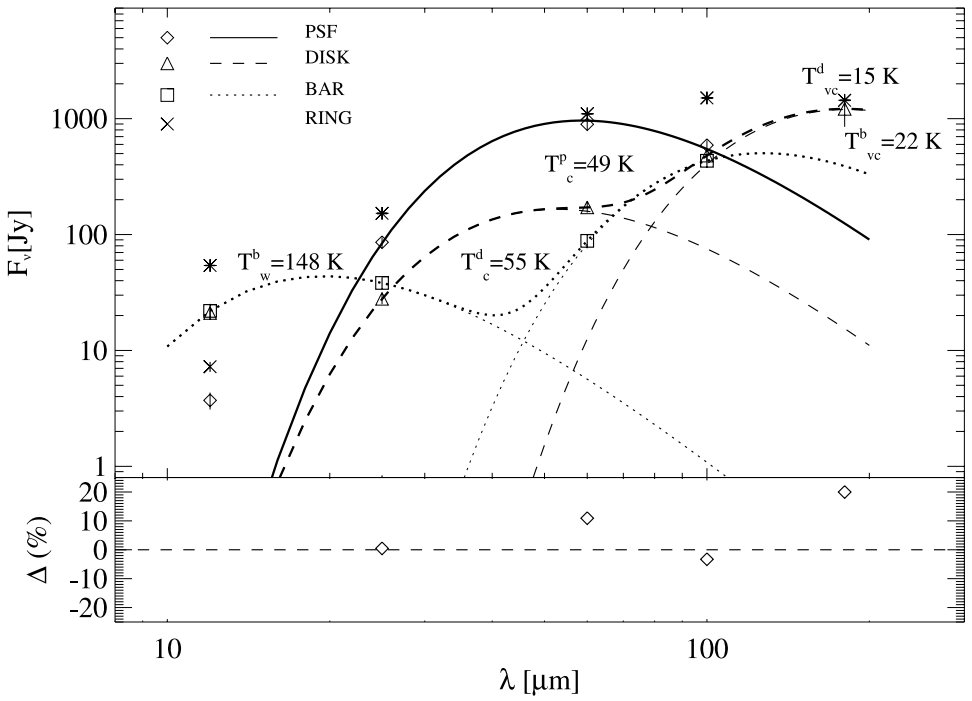

FIG. 7.—SED of the morphological components. The SED of the disk (*dashed line*) is modeled as the emission of two blackbodies with $T \sim 55$ and $\sim$15 K. The SED of the nuclear component (*dot-dashed line*) corresponds to a blackbody of $T \sim 50$ K. The SED of the bar (*dotted line*) is decomposed into two components, peaking at $T \sim 150$ and $\sim$22 K. In the bottom panel, we present the residuals between the sum of models and the total emission at each wavelength. There is a large residual at 12 μm, because there the emission is mainly attributed to PAHs and very small grains, which are in thermal equilibrium.

nent is typical of dust heated by dilute interstellar radiation. This very cold dust has been observed in normal galaxies (Walterbos & Greenawalt 1996; Walterbos & Schwering 1987; Cox, Krügel, & Mezger 1986) and in the disks of starburst and active galaxies (Radovich et al. 1999; Pérez García & Rodríguez Espinosa 2001).

The SED of the bar component can be modeled as the sum of two modified blackbodies, a warm one at $T = 148$ K and a cold one at $T = 22$ K. The origin of the warm component is related to regions of very intense star formation (Klaas et al. 1997; Lutz et al. 1996). Instead, the temperature of the cold component indicates an origin at a quiescent interstellar gas region, where star formation activity is low.

Most of the emission from the ring is concentrated in the mid-IR range, from 12 to 25 μm; beyond this wavelength the emission cannot be reliably determined. The characteristics of the ring emission seem to indicate a dominant contribution of PAHs and very small grains, as already mentioned in § 3.1, indicative of photodissociation regions.

4. DERIVED PHYSICAL PROPERTIES

4.1. *IR Luminosities*

We have computed the IR luminosities between 1 and 1000 μm for each morphological component (except for the ring, for the reasons mentioned in the previous section). The luminosity of each morphological component can be easily computed after the blackbody model is found. The resulting values are compiled in Table 2; the total values are obtained as the sum over all structural components.

The unresolved nuclear component is the most important contributor to the total IR luminosity, accounting for about half of the total emission. The disk accounts for $\sim$30% of the total, of which $\frac{2}{3}$ corresponds to the very cold component. The remaining $\sim$20% comes from the bar structure, in which the cold component dominates. The contribution of the ring to the total luminosity is very small.

4.2. *Star Formation Rate*

Star formation rates (SFRs) were calculated following Kennicutt (1998) for both the warm and cold components, using the expression

$$\mathrm{SFR} = 1.7 \times 10^{-10} L_{\mathrm{IR}}/L_\odot \quad \left(M_\odot\ \mathrm{yr}^{-1}\right).$$

This relationship applies only to relatively young starbursts, which implies that it only produces meaningful results when $T_{\mathrm{dust}} \gtrsim 25$ K. The resulting values are compiled in Table 2. As expected, the maximum star formation activity is taking place in the nuclear region at a moderate rate, $\sim$3.5 $M_\odot$ yr^{-1}. Furthermore, star formation activity at a lower rate is taking place in both the disk and the bar. The total SFR in the galaxy is 5.0 $M_\odot$ yr^{-1}. This value is 20% lower than that found by Radovich et al. (2001), who give a total SFR value of 6.1 $M_\odot$ yr^{-1} (after correcting their value for the different distance used herein). Note that Radovich et al. (2001) include the 20 K dust emission to complete the global SFR. We therefore consider the value provided here a rather more precise value. If we compare this value (4.97 $M_\odot$ yr^{-1}) with that obtained from the Hα emission by Hoopes et al. (1996), SFR = 0.6192 $M_\odot$ yr^{-1}, we estimate that the Hα emission must be obscured by a factor of $\sim$8, in good agreement with the value estimated by Hoopes et al. (1996).

4.3. *Dust Masses*

Dust masses were estimated, following Hildebrand et al. (1977), for the emissivity index ($\beta = 2$) used here, assuming

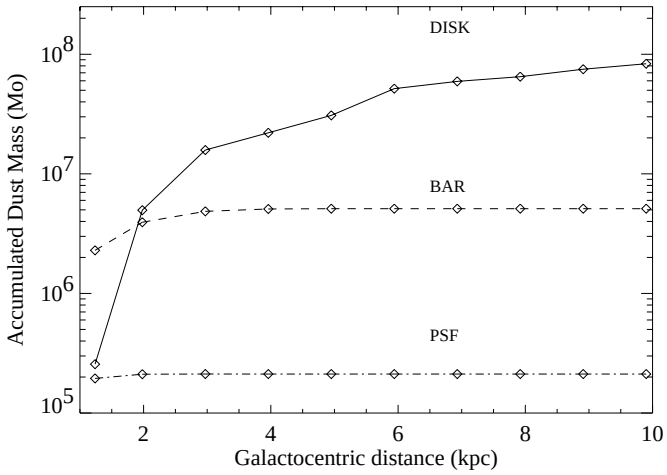

FIG. 8.—Variation along the semimajor axis of the accumulated mass for each morphological component: *solid line*, disk; *dashed line*, bar; *dot-dashed line*, PSF. The errors in the disk and PSF data are of the order of the size of the symbols used. The errors of the bar are, however, fairly large ($\sim 1.3 \times 10^7\ M_\odot$) and are not plotted, to avoid making the graph look confusing.

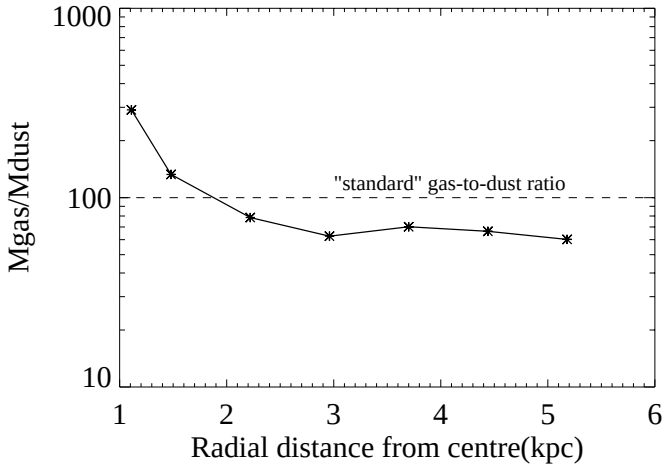

FIG. 9.—Radial variation of gas-to-dust mass ratio. For each radius the dust mass is the sum of the dust masses of all morphological components (PSF + disk + bar).

dust grain properties as in Hildebrand (1983):

$$M_d = 3.6 \times 10^{-5} (T_K/40)^{-6} L_{\rm IR}/L_\odot \quad (M_\odot).$$

The computed values for each component are shown in Table 2. The total dust mass of the galaxy is computed as the sum of all contributions. The most important contribution (about 94%) to the total mass comes from the very cold dust present in the disk. The mass estimate depends on the emissivity law adopted; we have checked that for the emissivity index 1, the resulting mass varies by a factor of 0.7–2 for dust temperatures in the range 18–65 K. We have also investigated the radial distribution of the dust mass by integrating over elliptical annuli at a given radius. The cumulative distribution per component is plotted in Figure 8. It can be seen that about half of the total dust mass of the galaxy is contained in the first 4′–5′.

The total dust mass value thus estimated gives a more reliable value than that obtained from the global SED. As an exercise, we have computed the mass using the integrated emission of the galaxy. For that purpose, the SED has been modeled as dust emission from a cold ($T \simeq 54$ K) and a very cold ($T \simeq 20$ K) component. In this way, we derive a total luminosity of $(3.68 \pm 0.02) \times 10^{10}\ L_\odot$ and total dust mass of $(2.92 \pm 0.04) \times 10^7\ M_\odot$, which are in agreement with the total values obtained for the whole galaxy by Radovich et al. (2001) (once the difference in distance has been allowed for). Note that this value is $\sim$3 times smaller than the dust mass obtained with the multiple-component approach.

We have also computed the gas-to-dust mass ratio for different galactocentric distances, using gas mass data from the literature (Scoville et al. 1985). The result is plotted in Figure 9. The mass ratio decreases strongly toward the outer part of the galaxy, approaching the canonical value of our Galaxy. In our Galaxy the gas-to-dust mass ratio is $\sim$160 (Sodroski et al. 1994). Devereux & Young (1990) obtained a value of 1070 for the inner disk (the inner half of the optical disk, 6.8 kpc) of NGC 253 using *IRAS* data. They concluded that this value is too high and would indicate that $\sim$80%–90% of the dust mass in spiral galaxies is radiating at $\lambda > 100\ \mu$m. At 5.2 kpc from the center, using our dust mass estimate, we obtain a value of $\sim$60. Furthermore, Houghton et al. (1997) provided values for molecular and atomic hydrogen for $R \leq 5.6$ kpc, the total hydrogen mass being $2.4 \times 10^9\ M_\odot$. We find that the global gas-to-dust mass ratio is $\sim$30, which is close to the outermost value in Figure 9.

Summarizing, we find that the gas-to-dust mass ratio varies greatly along the galaxy, from a value of 300 at 1 kpc to $\sim$60 in the outermost part. The dust mass appears to be distributed toward the outer parts of the galaxy and is rather difficult to detect at $\lambda \leqslant 100\ \mu$m, because of the very low temperature. The gas-to-dust mass ratio seems to indicate little excess of dust as compared to the canonical value in our Galaxy.

5. SUMMARY AND CONCLUSIONS

We have used ISOPHOT 180 μm and *IRAS* maps to study the spatial distribution of the far-IR emission in NGC 253. We have performed an analysis of the radial brightness profiles in terms of morphological components, reaching the following conclusions:

1. The radial light profiles show different extensions for the emission at the different wavelengths. The profiles from 12 to 100 μm show a central peak, reflecting the nuclear concentration of warm dust due to the starburst activity. On the outer parts, the profiles correspond to an exponential disk. At 180 μm the slope is rather flat and corresponds to an exponential disk. The decay of the light profile at 180 μm is comparable to that seen in the optical (B band). An extended cold dust halo is revealed in the 180 μm map. Marginal evidence is also found at 100 μm.

2. We have identified three main structures: an unresolved nuclear component, which corresponds to the central starburst, a bar, and an exponential disk. In addition, we have identified a ring at 12 and 25 μm.

3. The scale length of the disk is about 3.6 kpc and is very similar in all the bands studied. In all filters (12, 25, 60, and 100 μm) we obtained the same asymptotic limiting values for the ellipticity and the position angle: $\epsilon \simeq 0.79 \pm 0.10$ and P.A. $\simeq 52^\circ \pm 7^\circ$. These values are in good agreement with

those derived from optical images. We conclude that the scale lengths of both the stars and the dust are similar.

4. The disk can be characterized by dust emission at two temperatures: a warm component, with dust temperature of $\sim$55 K, and a very cold component, with temperature of $\sim$16 K. The first component results from dust heated by star-forming regions in the galaxy disk, while the very cold dust is heated by the interstellar radiation field. This work confirms the presence of a large amount of cold dust in the disk of NGC 253, which contains $\sim$94% of the overall dust mass. The estimated total dust mass is $8.2 \times 10^7\ M_\odot$.

5. We could identify in all the light profiles an unresolved nuclear source, which was modeled as the PSF of the corresponding filter. The SED of this component could be modeled as blackbody emission at $\sim$50 K. The dust is heated by the intense radiation field produced in the nuclear starburst.

6. A far-IR bar has also been detected and characterized. This bar had been previously detected in the near-IR. The bar P.A. (69°.5) and its extent are in agreement with those of the near-IR bar. The SED of the bar could be modeled with two components, a warm dust component at $\sim$148 K and a cold dust component at $\sim$23 K.

7. In the light profiles at 12 and 25 μm, we could identify a ring structure visible at 3 kpc, coincident with the end of the bar. The IR color profiles indicate the presence of PAHs at the end of the bar and coincident with the position of the ring. The detection of the ring had been previously claimed from both molecular gas (CO) and Hα imaging.

8. The total IR luminosity computed for NGC 253 is $4 \times 10^{10}\ L_\odot$. About half of the total luminosity corresponds to the unresolved central component, 31% comes from the disk, and 17% comes from the bar.

9. The total SFR in NGC 253 is about 5.0 $M_\odot\ \mathrm{yr}^{-1}$. About 70% comes from the nuclear starburst, and the rest comes from the disk and the bar. Estimates of the star formation rates derived from Hα photometry are a factor of $\sim$10 below our estimate, which is consistent with previous estimates for optical extinction.

10. The gas-to-dust mass ratio varies appreciably throughout the galaxy, from a value 300 in the inner part to $\sim$60 in the outermost part. Globally, NGC 253 seems to be a dust-rich galaxy, contrary to what was found in previous studies.

We thanks an anonymous referee for his very helpful and detailed report, which greatly improved our paper. This project has been partly funded by the Spanish DGI (AYA2001-3939-C03-03). We express our thanks to Antonia María Varela for her comments and fruitful discussions. Thanks are due to Professor John Beckman for reading of the text. We also acknowledge the Scientific Editorial Service of the IAC for corrections.

IPAC is operated by the Jet Propulsion Laboratory (JPL) and California Institute of Technology (Caltech) for NASA. IPAC is funded by NASA as part of the *IRAS* extended mission program under contract to JPL/Caltech. The *COBE* data sets were developed by the NASA Goddard Space Flight Center under the guidance of the *COBE* Science Working Group and were provided by the NSSDC.

REFERENCES

Alton, P. B., Davies, J. I., & Trewhella, M. 1998a, MNRAS, 296, 773
Alton, P. B., et al. 1998b, A&A, 335, 807
Aumann, H. H., Fowler, J. W., & Melnyk, M. 1990, AJ, 99, 1674
Bianchi, S., Davies, J. I., & Alton, P. B. 2000, A&A, 359, 65
Buta, R. 1996, in IAU Colloq. 157, Barred Galaxies, ed. R. Buta, D. A. Crocker, & B. G. Elmegreen (ASP Conf. Ser. 91; San Francisco: ASP), 11
Chini, R., Krügel, E., & Kreysa, E. 1992, A&A, 266, 177
Cox, R., Krügel, E., & Mezger, P. G. 1986, A&A, 155, 380
Davies, J. I., Trewhella, M., Jones, H., Lisk, C., Madden, A., & Moss, J. 1997, MNRAS, 288, 679
Devereux, N. A., Price, R., Wells, L. A., & Duric, N. 1994, AJ, 108, 1667
Devereux, N. A., & Young, J. S. 1990, ApJ, 359, 42
Devriendt, J. E. G., Guiderdoni, B., & Sadat, R. 1999, A&A, 350, 381
Disney, M. J., Davies, J., & Phillipps, S. 1989, MNRAS, 239, 939
Dudley, C. C., & Wynn-Williams, C. G. 1999, MNRAS, 304, 549
Efstathiou, A., Rowan-Robinson, M., & Siebenmorgen, R. 2000, MNRAS, 313, 734
Engargiola, G. 1991, ApJS, 76, 875
Engargiola, G., & Harper, D. A. 1992, ApJ, 394, 104
Forbes, D. A., & DePoy, D. I. 1992, A&A, 259, 97
Gabriel, C., Acosta-Pulido, J. A., Heinrichsen, I., Skaley, D., Morris, H., & Tai, W.-M. 1997, in ASP Conf. Ser. 125, Astronomical Data Analysis Software and Systems VI, ed. G. Hunt & H. E. Payne (San Francisco: ASP), 108
Haas, M., Lemke, D., Stickel, M., Hippelein, H., Kunkel, M., Herbstmeier, U., & Mattila, K. 1999, in The Universe as seen by *ISO*, ed. P. Cox & M. F. Kessler (ESA SP-427; Noordwijk: ESTEC), 885
Helou, G. 1986, ApJ, 311, L33
———. 2000, in Infrared Space Astronomy, Today and Tomorrow, ed. F. Casoli, J. Lequeux, & F. David (Berlin: Springer), 337
Hildebrand, R. H. 1983, QJRAS, 24, 267
Hildebrand, R. H., Whitcomb, S. E., Winston, R., Stiening, R. F., Harper, D. A., & Moseley, S. H. 1977, ApJ, 216, 698
Hoopes, C. G., Walterbos, R. A. M., & Greenawalt, B. E. 1996, AJ, 112, 1429
Houghton, S., Whiteoak, J. B., Koribalski, B., Booth, R., Wiklind, T., & Wielebinski, R. 1997, A&A, 325, 923
Jedrzejewski, R. I. 1987, MNRAS, 226, 747
Kennicutt, R. C., Jr. 1998, ARA&A, 36, 189
Keto, E., Hora, J. L, Fazio, G. G., Hoffmann, W., & Deutsch, L. 1999, ApJ, 518, 183
Klaas, U., Haas, M., Heinrichsen, I., & Schulz, B. 1997, A&A, 325, L21
Knapp, G. R., Rupen, M. P., Fich, M., Harper, D. A., & Wynn-Williams, C. G. 1996, A&A, 315, L75
Lemke, D., et al. 1996, A&A, 315, L64
Lutz, D., et al. 1996, A&A, 315, L137
Mayya, Y. D., & Rengarajan, T. N. 1997, AJ, 114, 946
Pence, W. D. 1980, ApJ, 239, 54
Pérez García, A. M., Melo V. P., Acosta-Pulido, J. A., Muñoz-Tuñón, C., & Rodríguez Espinosa, J. M. 2001, Ap&SS Suppl., 277, 347
Pérez García, A. M., & Rodríguez Espinosa, J. M. 2001, ApJ, 557, 39
Pietsch, W., Vogler, A., Klein, U., & Zinnecker, H. 2000, A&A, 360, 24
Prieto, M., Gottesman S. T., Aguerri, J.-A. L., & Varela, A.-M. 1997, AJ, 114, 1413
Puche, D., & Carignan, C. 1991, ApJ, 378, 487
Radovich, M., Kahanpää, J., & Lemke, D. 2001, A&A, 377, 73
Radovich, M., Klaas, U., Acosta-Pulido, J., & Lemke, D. 1999, A&A, 348, 705
Rice, W. 1993, AJ, 105, 67
Rowan-Robinson, M., & Crawford, J. 1989, MNRAS, 238, 523
Sandage, A., & Tammann, G. A. 1975, ApJ, 196, 313
Scoville, N. Z., Soifer, B. T., Neugebauer, G., Young, J. S., Matthews, K., & Yerka, J. 1985, ApJ, 289, 129
Silva, L., Granato, G. L., Bressan, A., & Danese, L. 1998, ApJ, 509, 103
Sodroski, T. J., et al. 1994, ApJ, 428, 638
Sorai, K., Nakai, N., Kuno, N., Nishiyama, K., & Hasegawa, T. 2000, PASJ, 52, 785
Telesco, C. M. 1993, in Infrared Astronomy, ed. A. Mampaso, M. Prieto, & F. Sánchez (Cambridge: Cambridge Univ. Press), 175
Walterbos, R. A. M., & Greenawalt, B. 1996, ApJ, 460, 696
Walterbos, R. A. M., & Schwering, P. B. W. 1987, A&A, 180, 27
Xilouris, E. M., Byun, Y. I., Kylafis, N. D., Paleologou, E. V., & Papamastorakis, J. 1999, A&A, 344, 868
Xu, C., & Helou, G. 1996, ApJ, 456, 163